RESEARCH ARTICLE

National Science Open
5: 20250075, 2026
https://doi.org/10.1360/nso/20250075

Earth and Environmental Sciences

Special Topic: Frontiers of Stable Isotope Research

Sulfur isotope difference between evaporites and carbonates reveals oxidation of early Paleozoic ocean

Tianzheng Huang[1,2] & Bing Shen[1,*]

[1]*Key Laboratory of Orogenic Belt and Crustal Evolution, MOE; School of Earth and Space Sciences, Peking University, Beijing 100871, China;*
[2]*School of Physics, Peking University, Beijing 100871, China*

*Corresponding author (email: bingshen@pku.edu.cn)

Received 13 November 2025; Revised 21 December 2025; Accepted 29 January 2026; Published online 2 February 2026

Abstract: The extent of sulfidic (anoxic and H_2S rich) seafloor, an important ocean redox indicator, can be constrained by the redox sensitive elements (RSE, e.g., Mo, U, V) contents and their isotopes in black shales. Although the sulfidic seafloor was at least sporadic and episodic and the ocean remained incompletely oxidized until the Paleozoic oxygenation event (POE) at 400–300 Ma, it is unclear whether the ocean was gradually oxidized or remained modest oxygenation followed by a stepwise oxidation in POE. In this study, we compiled published sulfur (S) isotopes of evaporitic sulfate ($\delta^{34}S_{Eva}$) and carbonate associated sulfate (CAS, $\delta^{34}S_{CAS}$) to the refine the ocean redox evolution in the past 600 Ma. The statistic difference between $\delta^{34}S_{Eva}$ and $\delta^{34}S_{CAS}$ ($\Delta_{Eva\text{-}CAS} = \delta^{34}S_{Eva} - \delta^{34}S_{CAS}$) reflects a gradual shrinkage of sulfidic seafloor and weakening of VOSC (volatile organosulfur compounds) cycle before POE, while the exclusive negative $\Delta_{Eva\text{-}CAS}$ values after 300 Ma indicates the thorough ocean oxygenation that muted the VOSC cycle.

Keywords: volatile organosulfur compounds, evaporite, carbonate associated sulfate, redox landscape, oxygenation event

INTRODUCTION

Sulfur (S) is one of the major redox-sensitive elements in Earth's surface, and the S cycle, represented by the coupled sulfate reduction and sulfide oxidation, played the key role in modulating the surface Earth redox landscape since at least 2.5 Ga (billion years ago) [1]. As such, the deep time S cycle has been investigated to retrieve redox evolution of the ocean-atmosphere system [2,3]. It is widely accepted that the extent of sulfidic/euxinic (anoxic and H_2S rich) seafloor is an important manifestation of ocean redox condition. For example, the widespread sulfidic continental margins in the mid-Proterozoic (1.8–0.8 Ga) oceans might have retarded the evolution of eukaryotes in the context low atmospheric pO_2 level [4–6], whereas dramatic shrinkage of sulfidic seafloor in the aftermath of Marinoan snowball Earth glaciation (~650–635 Ma, million years ago), reflecting the second rise of atmospheric pO_2 level and ocean oxidation, i.e., the Neoproterozoic Oxygenation Event (NOE), might have paved the way for the diversification of eukaryotes and the rise of animals [7,8]. The extent of sulfidic seafloor can be quantified by the concentrations of redox sensitive

© The Author(s) 2026. Published by Science Press and EDP Sciences. This is an Open Access article distributed under the terms of the Creative Commons Attribution License (https://creativecommons.org/licenses/by/4.0), which permits unrestricted use, distribution, and reproduction in any medium, provided the original work is properly cited.

elements (RSE, e.g., Mo, U, V) in black shale. Low RSE contents reflect the scavenge of RSE in seawater when sulfidic seawater covers 1%–10% of seafloor [9]. However, when the sulfidic seafloor reduced below the threshold of 1%, such as in Phanerozoic, RES proxies are less sensitive to redox landscape. For this reason, although the oceans were not completely oxidized until POE, it remains unclear whether the ocean was gradually oxidized or experienced a stepwise oxygenation in POE.

To refine the redox evolution of Phanerozoic oceans (e.g., the extent of sulfidic seafloor), we revise the marine S cycle by incorporating the marine organosulfur cycle. Recent studies of the modern marine S cycle indicate, organosulfur compounds, more specifically, VOSC (volatile organosulfur compounds), including dimethylsulfide (DMS) and methysulfide (MS), represents an important and active yet poorly-known component in the modern S cycle [10–13]. VOSC could be generated in two pathways. In the modern ocean, VOSC mainly derives from decompositions of dimethylsulfoniopropionate (DMSP), an intermediate product in the assimilatory sulfate reduction of phytoplanktons, i.e., the DMSP pathway [14]. It is estimated that, although more than 99% of DMSP-derived VOSC is either decomposed or consumed by microbes, the annual flux from the ocean to the atmosphere is ~1 Tmol [11], accounting for ~1/3 of terrestrial sulfate input [1]. Alternatively, VOSC could also be generated through the direct reaction of dissolved organic carbon (DOC) with H_2S in organic-rich modern sulfidic lakes, i.e., the H_2S methylation pathway [15]. Thus, the revised S cycle should include three S components, i.e., sulfate, sulfide, and organosulfur (e.g., VOSC).

Unravelling the global S cycle has been approached with S isotopes [1]. The DMSP and H_2S methylation pathways have distinct isotopic effect. VOSC production via the DMSP pathway does not fractionate S isotopes [11], therefore the VOSC cycle in the modern surface oceans does not modify the seawater sulfate S isotopic composition ($\delta^{34}S_{SW}$) [16]. This may explain the huge VOSC flux (1 Tmol/year) from the ocean to the atmosphere has long been ignored in ancient S cycle [1]. In contrast, VOSC from the H_2S methylation pathway inherits the ^{34}S-depleted isotopic signal of H_2S [15]. Thus, emission of VOSC that derives from the H_2S methylation preferentially removes ^{32}S from the aqueous environment and potentially generates a depth gradient of S isotopes for both H_2S ($\delta^{34}S_{H_2S}$) and sulfate ($\delta^{34}S_{SO_4}$) in the water column. This mechanism has been used to explain the global precipitation of "superheavy pyrite" in the non-glacial interlude (660–650 Ma) of Cryogenian Snowball Earth glaciations, a time with widespread sulfidic continental margins [17]. Concurrently, VOSC oxidation in the atmosphere and precipitation of ^{34}S-depleted sulfate aerosols to other regions could maintain a lateral gradient of $\delta^{34}S_{SW}$, in sharp contrast with homogeneous $\delta^{34}S_{SW}$ of the modern ocean [1,2,11]. Therefore, VOSC formation via the H_2S methylation pathway could be traced by the S isotope records.

In this study, we reconstruct the evolutionary history of the VOSC cycle in the past 600 million years so as to constrain the extent of sulfidic seafloor in continental margins. Because active VOSC cycle (via H_2S methylation) would generate both vertical and lateral $\delta^{34}S_{SW}$ gradients [17,18], the extent/intensity of VOSC cycle could be inferred from the $\delta^{34}S_{SW}$ records.

METHOD AND MODEL

S isotope statics

S isotope of carbonate associated sulfate ($\delta^{34}S_{CAS}$) and evaporite ($\delta^{34}S_{Eva}$) in 0–600 Ma are divided in to 12

bins of 50 Ma. All data are from Crockford *et al*. [19] and references therein. $\delta^{34}S_{CAS}$ data includes $\delta^{34}S$ from lithologies of carbonate. Phosphorites $\delta^{34}S$ are merged into $\delta^{34}S$ statistics due to similar origins and limited data volume. And $\delta^{34}S_{Eva}$ data includes $\delta^{34}S$ from lithologies of gypsum and anhydrite.

Bootstrapping and Two-sample heteroscedasticity *T*-test are performed in each bin. Bootstrapping is done using statical software Past. Data in each bin are resampled 9999 times and averages are calculated for each resampling. The minimum, maximum, and average of averages are recorded (Table S1) and plotted in Figure 1b. Two-sample heteroscedasticity *T*-test is performed using Excel (Table S1).

S isotope of pyrite ($\delta^{34}S_{py}$) data is entirely sourced from Canfield and Farquhar [20] and references cited therein.

Model structure

Model descriptions

A steady state 1D-DAR model is developed to simulate Dissimilatory Sulfate Reduction (DSR), H_2S oxidation, pyrite formation and volatile organosulfur compound (VOSC) formation in sulfidic seawater or sulfidic porewater in sediments. The parameters in seawater and porewater differ significantly. For simplicity, all parameters are shown in Table S2 and values are not shown in text.

A water column or porewater column of z_L meters depth is divided into 2000 differential layers with depth of dz. The concentrations of sulfate ([SO_4]), [H_2S], [O_2], and Fe^{2+} ([Fe]) are considered in each differential layer. The concentration of components is affected by diffusion, advection, and reactions as indicated by the governing equation (Eq. (1)):

$$\frac{\partial[X]}{\partial t} = D_X\left(\frac{\partial^2[X]}{\partial z^2}\right) + s\left(\frac{\partial[X]}{\partial z}\right) + \mathrm{sms}(X), \tag{1}$$

where X refers to a component in [$^{32}SO_4$], [$^{34}SO_4$], [$H_2^{32}S$], [$H_2^{34}S$], [O_2], [Fe] and particle organic carbon (POC, [CH_2O]). D_X is the diffusion constant for X and s is the advection rate of X. Sedimentation process is simulated by a slow downward advection in porewater simulation. sms(X) refers to the chemical reaction rate of X.

Reactions including DSR (Eq. (2)), H_2S oxidation (Eq. (3)), pyrite formation (Eq. (4)) and VOSC formation (Eq. (5)) are considered in the model.

$$SO_4^{2-} + 2CH_2O \dashrightarrow H_2S, \tag{2}$$

$$H_2S + 2O_2 \dashrightarrow SO_4^{2-}, \tag{3}$$

$$2H_2S + Fe \dashrightarrow FeS_2\downarrow, \tag{4}$$

$$H_2S \dashrightarrow \mathrm{VOSC}\uparrow. \tag{5}$$

All S in Eqs. (2)–(5) refers to both ^{32}S and ^{34}S. This model focuses on how VOSC and pyrite formation affect seawater sulfur isotopes. While both reaction rates are influenced by other components—such as DOC and reactive Fe—accounting for these substances only introduces a secondary factor: the spatial distribution of VOSC and pyrite formation. Regarding the two core factors—whether VOSC and pyrite form, and how much—using a fixed reaction rate constant produces essentially the same results as explicitly calculating formation rates from DOC and reactive Fe concentration distributions. Thus, we assume that dissolved

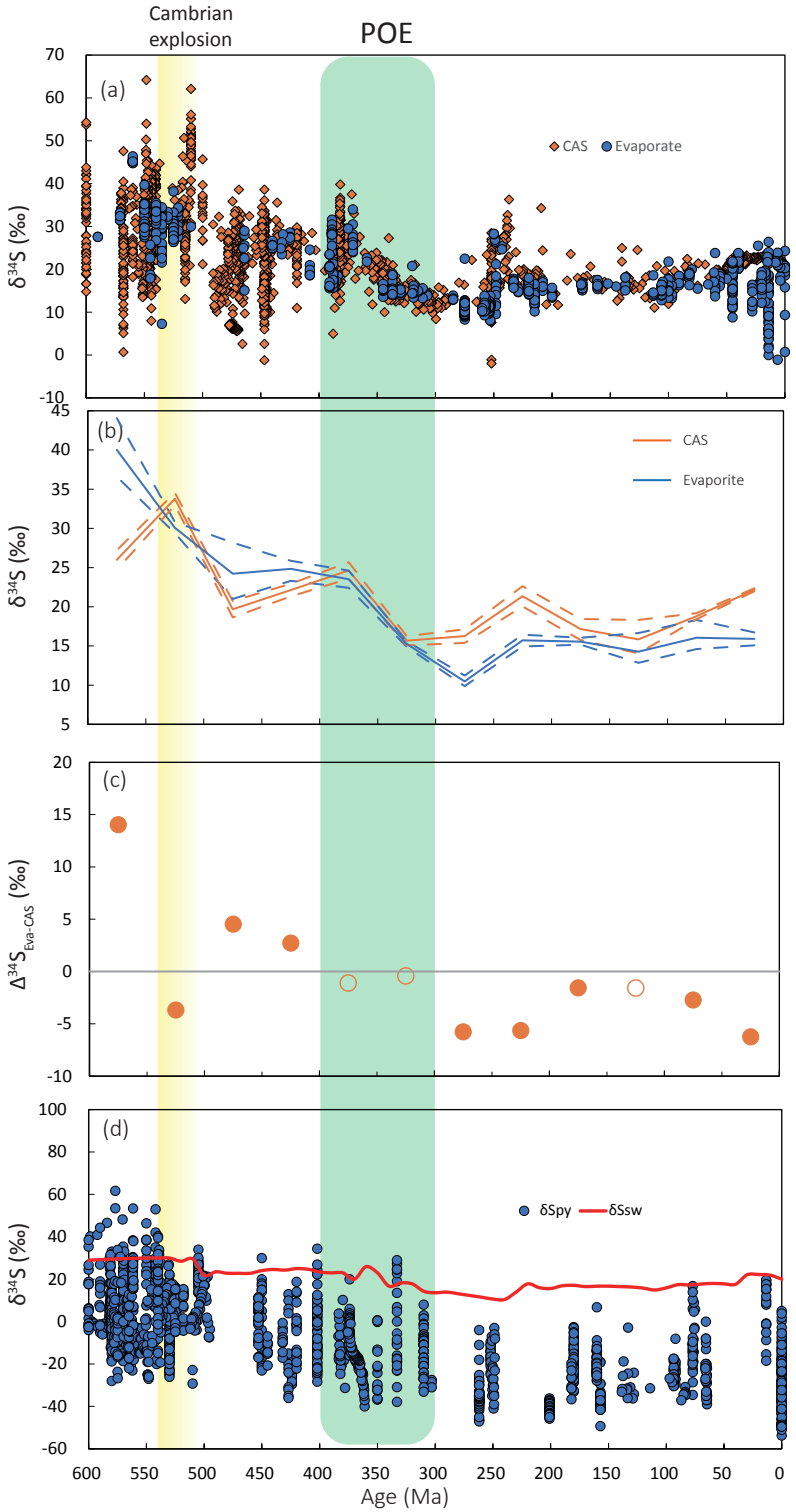


Figure 1 Statistic results of $\delta^{34}S_{Eva}$ and $\delta^{34}S_{CAS}$ [19] and $\delta^{34}S_{py}$ [20] in 0–600 Ma. The green bar represents the POE [36]. (a) $\delta^{34}S_{Eva}$ and $\delta^{34}S_{CAS}$ data in 0–600 Ma. (b) The Average of $\delta^{34}S_{Eva}$ and $\delta^{34}S_{CAS}$ by bootstrapping (9999 times) in each 50 million years (Myr) bins. Dotted lines represent the upper and lower limit of the average of $\delta^{34}S_{Eva}$ and $\delta^{34}S_{CAS}$ in bootstrapping. Solid lines represent the average of original data. (c) The difference between $\delta^{34}S_{Eva}$ and $\delta^{34}S_{CAS}$ in each 50 Myr bins. Open cycles mean no statical significant and solid cycles are statical significant with a *T*-test. (d) $\delta^{34}S_{py}$ data in 0–600 Ma comparing with $\delta^{34}S_{SW}$ [20]. $\delta^{34}S_{py}$ larger than $\delta^{34}S_{SW}$ means "superheavy pyrite".

organic carbon (DOC) is superfluous to form VOSC, thus consumption of DOC is not considered in the model.

The rates of Chemical reactions can be expressed as (Eqs. (6)–(12)):

$$\mathrm{sms}\left({}^{32}\mathrm{SO_4}\right) = -R_{\mathrm{DSR}}^{32} * \left[{}^{32}\mathrm{SO_4}\right] * [\mathrm{CH_2O}] + R_{\mathrm{OX}} * \left[\mathrm{H_2^{32}S}\right] * [\mathrm{O_2}], \tag{6}$$

$$\mathrm{sms}\left({}^{34}\mathrm{SO_4}\right) = -R_{\mathrm{DSR}}^{34} * \left[{}^{34}\mathrm{SO_4}\right] * [\mathrm{CH_2O}] + R_{\mathrm{OX}} * \left[\mathrm{H_2^{32}S}\right] * [\mathrm{O_2}], \tag{7}$$

$$\mathrm{sms}\left(\mathrm{H_2^{32}S}\right) = -R_{\mathrm{OX}} * \left[\mathrm{H_2^{32}S}\right] * [\mathrm{O_2}] - R_{\mathrm{PY}} * \left[\mathrm{H_2^{32}S}\right] * [\mathrm{Fe}] - R_{\mathrm{VOSC}} * \left[\mathrm{H_2^{32}S}\right], \tag{8}$$

$$\mathrm{sms}\left(\mathrm{H_2^{34}S}\right) = -R_{\mathrm{OX}} * \left[\mathrm{H_2^{34}S}\right] * [\mathrm{O_2}] - R_{\mathrm{PY}} * \left[\mathrm{H_2^{34}S}\right] * [\mathrm{Fe}] - R_{\mathrm{VOSC}} * \left[\mathrm{H_2^{34}S}\right], \tag{9}$$

$$\mathrm{sms}(\mathrm{O_2}) = -R_{\mathrm{OX}} * \left[\mathrm{H_2^{32}S}\right] * [\mathrm{O_2}] - R_{\mathrm{OX}} * \left[\mathrm{H_2^{34}S}\right] * [\mathrm{O_2}], \tag{10}$$

$$\mathrm{sms}(\mathrm{Fe}) = -R_{\mathrm{PY}} * \left[\mathrm{H_2^{32}S}\right] * [\mathrm{Fe}] - R_{\mathrm{PY}} * \left[\mathrm{H_2^{34}S}\right] * [\mathrm{Fe}], \tag{11}$$

$$\mathrm{sms}(\mathrm{CH_2O}) = -R_{\mathrm{DSR}}^{32} * \left[{}^{32}\mathrm{SO_4}\right] * [\mathrm{CH_2O}] - R_{\mathrm{DSR}}^{34} * \left[{}^{34}\mathrm{SO_4}\right] * [\mathrm{CH_2O}], \tag{12}$$

where R refers to reaction rate constant. The subscripts DSR, OX, PY, VOSC are DSR reaction, H_2S oxidation reaction, pyrite formation and VOSC formation reactions respectively. The superscripts 32 and 34 refers to ^{32}S and ^{34}S. S isotope fractionation in DSR is shown by $\Delta_{\mathrm{DSR}} = \left(R_{\mathrm{DSR}}^{32} / R_{\mathrm{DSR}}^{34} - 1\right) \times 1000$. Other reactions do not involve S isotope fractionation.

The upper boundary is a free boundary that exchanges with non-sulfidic seawater. Upper boundary conditions include seawater sulfate concentration ($[SO_4]_0$) and $\delta^{34}S_{SW}$, $[O_2]_0$ and POC input ($[CH_2O]_0$). The concentrations of the other components are 0 in seawater. The lower boundary is a closed boundary for all components except for [Fe]. There is benthic flux of Fe^{2+} in seawater column by setting a lower boundary Fe^{2+} concentration ($[Fe]_0$). In sediment porewater, we assume sufficient Fe supply from active Fe in sediments, thus [Fe] in all differential layers are set as $[Fe]_0$ in porewater column.

The simulation begins with an initial condition that concentrations of all components are 0 in the entire water column. Different initial conditions don't affect the final results. The simulation process is a temporal iteration process to the steady state. The steady state refers to when the maximum variation ratio of each component in all differential layers in an iteration is less than 10^{-10} ($\max(\mathrm{d}[X]/[X]) < 10^{-10}$).

Modelling results

Four scenarios are simulated: (1) Seawater without pyrite and VOSC formation. (2) Seawater without VOSC formation but with pyrite formation. (3) Seawater without pyrite formation with VOSC formation. (2) Sediment porewater without pyrite and VOSC formation. The profiles of sulfate, H_2S and total dissolved sulfur (TDS, all dissolved sulfur species, include sulfate and H_2S in this model) concentration and S isotopic composition of scenario 1–3 are shown in Figure 2 and scenario 4 is shown in Figure S1a and b. There is strictly no difference in [TDS] and $\delta^{34}S_{TDS}$ in scenario 1 in which only the circulation of DSR and H_2S oxidation happens. The conservativity is broken by pyrite and VOSC formation that removes H_2S from the system causing decrease of [TDS] and increase of $\delta^{34}S_{TDS}$ in scenario 2–3. Sediment porewater show different trends with seawater system. Even if no pyrite and VOSC formation, [TDS] decreases and $\delta^{34}S_{TDS}$

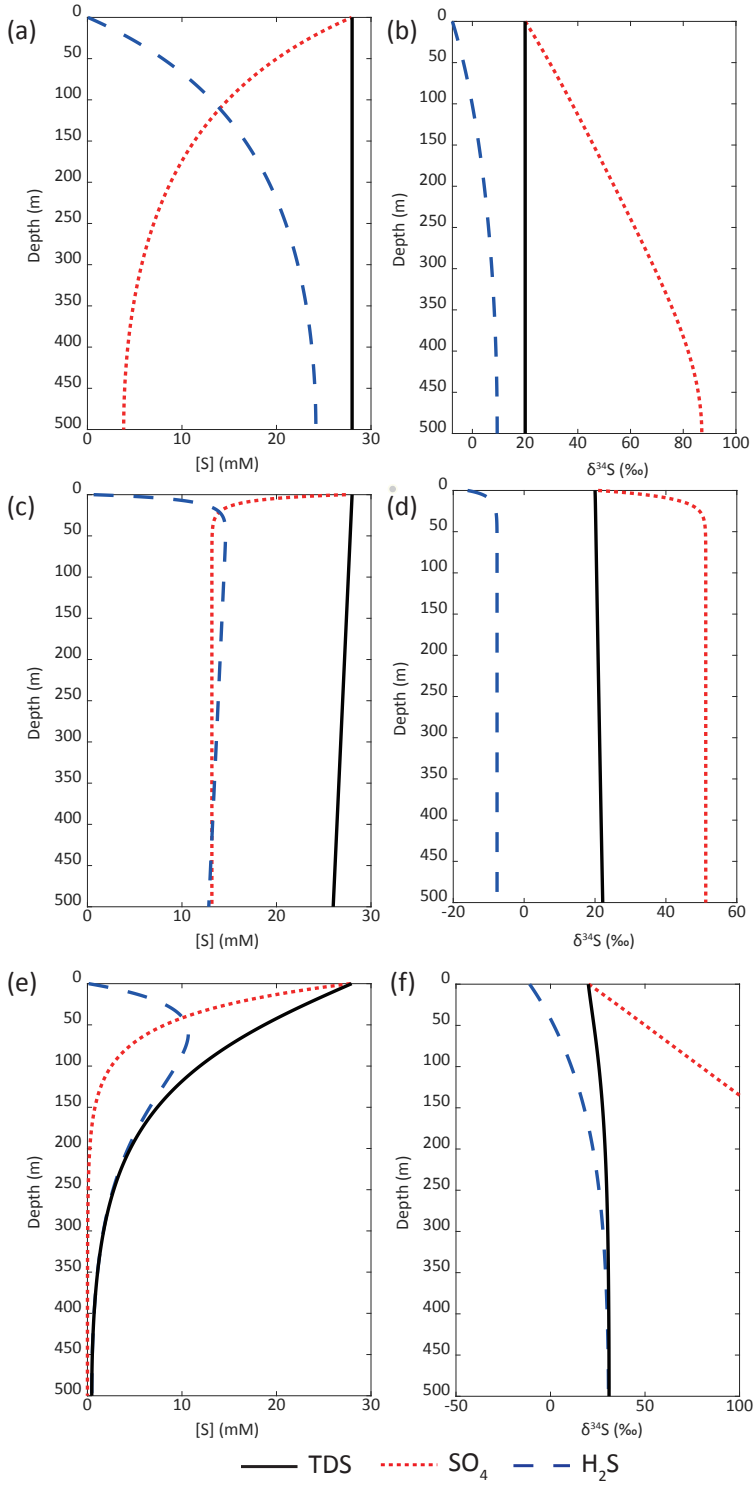


Figure 2 Modeling result of SO_4^{2-}, H_2S, and TDS in sulfidic seawater. (a, b) Concentration and isotope composition of SO_4^{2-}, H_2S, and TDS without pyrite sedimentation and VOSC formation. (c, d) Concentration and isotope composition of SO_4^{2-}, H_2S, and TDS with pyrite sedimentation and without VOSC formation. (e, f) Concentration and isotope composition of SO_4^{2-}, H_2S, and TDS without pyrite sedimentation and with VOSC formation. Both pyrite sedimentation and VOSC formation remove H_2S with $\delta^{34}S$ lower than $\delta^{34}S_{TDS}$ and increases $\delta^{34}S_{TDS}$.

increases from seawater to sediment porewater. This phenomenon is due to different diffusion constant for sulfate and H_2S in porewater. [TDS] and $\delta^{34}S_{TDS}$ are conservative if D_{SO_4} and D_{H_2S} are the same (Figure S1c and d), and the trend reversed if the value of D_{SO_4} and D_{H_2S} are exchanged (Figure S1e and f).

Mathematical proof

The main consequences of our model are that $\delta^{34}S_{TDS}$ is conservative in the circulation of DSR and H_2S oxidation and removing H_2S from the system by pyrite and VOSC formation increase $\delta^{34}S_{TDS}$. Additionally, a difference of D_{SO_4} and D_{H_2S} in porewater increases $\delta^{34}S_{TDS}$. These outcomes are qualitative, and there are too many parameters that need sensitivity tests to prove the consequences.

We made a mathematical proof to confirm that only external flux to TDS reservoir and differences between D_{SO_4} and D_{H_2S} can affect $\delta^{34}S_{TDS}$. Governing equation of $^{32}S_{TDS}$ and $^{34}S_{TDS}$ can be delivered by sum (Eq. (1)) when X refers to $^{32}SO_4$ and $H_2^{32}S$, or $^{34}SO_4$ and $H_2^{34}S$ as shown by (Eqs. (13) and (14))

$$\frac{\partial[^{32}\mathrm{TDS}]}{\partial t} = D_{^{32}SO_4}\left(\frac{\partial^2[^{32}SO_4]}{\partial z^2}\right) + D_{^{32}H_2S}\left(\frac{\partial^2[H_2^{32}S]}{\partial z^2}\right) + s\left(\frac{\partial[^{32}SO_4]}{\partial z}\right) + s\left(\frac{\partial[H_2^{32}S]}{\partial z}\right) - R_{PY} * [H_2^{32}S] * [Fe] - R_{VOSC} * [H_2^{32}S], \quad (13)$$

$$\frac{\partial[^{34}\mathrm{TDS}]}{\partial t} = D_{^{34}SO_4}\left(\frac{\partial^2[^{34}SO_4]}{\partial z^2}\right) + D_{^{34}H_2S}\left(\frac{\partial^2[H_2^{34}S]}{\partial z^2}\right) + s\left(\frac{\partial[^{34}SO_4]}{\partial z}\right) + s\left(\frac{\partial[H_2^{34}S]}{\partial z}\right) - R_{PY} * [H_2^{34}S] * [Fe] - R_{VOSC} * [H_2^{34}S]. \quad (14)$$

The reaction terms concerning the circulation of DSR and H_2S oxidation are eliminated in the sum, leaving only pyrite and VOSC formation. If pyrite and VOSC formation are prevented, the only way to alter the ratio of ^{32}TDS and ^{34}TDS is S flux in conversion between sulfate and H_2S. However, D_X and s for SO_4 and H_2S are identical in seawater. Since the upper boundary is the only open boundary for TDS and TDS is chemically conservative, there is no constant vertical TDS flux in seawater column in steady state. Therefore, TDS and $\delta^{34}S_{TDS}$ are conservative in the steady state. In sediment porewater, D_{SO_4} is smaller than D_{H_2S}. Thus, [H_2S] gradient is more efficient in diffusion exchange. When SO_4 is converted to H_2S, less TDS is required to maintain no TDS flux. As a result, [TDS] decreases and $\delta^{34}S_{TDS}$ increases with depth.

In conclusion, Eqs. (13) and (14) demonstrate that S isotope fractionation in DSR makes no change to [TDS] and $^{34}S_{TDS}$. Only external fluxes to TDS reservoir or difference of physical properties between SO_4 and H_2S can break the conservative of [TDS] and $^{34}S_{TDS}$. Because the only dissolved S species in non-sulfidic seawater is sulfate, S flux from sulfidic seawater inherits $\delta^{34}S_{TDS}$. The dissolved S flux always has $\delta^{34}S$ equals or higher than $\delta^{34}S_{SW}$. Thus, oxidation of H_2S from sulfidic seawater cannot explain the negative $\delta^{34}S_{SW}$ gradient in non-sulfidic seawater.

Sensitivity tests

In addition to the mathematical proof provided in Supplementary materials 3.3, we verified whether major

physical and chemical parameters such as DSR reaction rate, sulfur isotope fractionation in DSR, and turbulent diffusion constant would alter the core conclusion that total dissolved sulfur isotopes remain conservative under the premise of no gaseous or solid sulfur production. The results show that regardless of how the above physical and chemical parameters vary, changes in TDS concentration are always lower than 1×10^{-7} mmol/L, which might due to the residual error in steady state judgement (10^{-10} in 1 iteration), and changes in TDS sulfur isotopes are always far below the analytical precision of sulfur isotopes (0.05 permil) (see Table S3). Therefore, sensitivity tests demonstrate that variations in major physical and chemical parameters do not alter the core conclusions of this model.

RESULTS

In order to reconstruct the vertical (depth) $\delta^{34}S_{SW}$ gradients, we analyzed the compiled S isotope data of evaporite ($\delta^{34}S_{Eva}$) and carbonate associated sulfate (CAS, $\delta^{34}S_{CAS}$), both of which are believed to record $\delta^{34}S_{SW}$ [1,2,20]. Evaporite mainly precipitates in the near shore regions, mostly intertidal to supratidal environments or restricted basins and under the arid climatic conditions (i.e., precipitation < evaporation) [21]. In contrast, carbonate can precipitate in a wider range of environments, from shallow to deep water settings [22]. In the other word, the average depth of carbonate precipitation should be deeper than that of evaporite. Therefore, the mean $\delta^{34}S_{Eva}$ and $\delta^{34}S_{CAS}$ values record $\delta^{34}S_{SW}$ in the near-shore and open ocean environments, respectively, and their difference ($\Delta_{Eva\text{-}CAS} = \delta^{34}S_{Eva} - \delta^{34}S_{CAS}$) represents the depth gradient (from shallow to deep) of $\delta^{34}S_{SW}$.

Both $\delta^{34}S_{Eva}$ and $\delta^{34}S_{CAS}$ data of the past 600 Ma is grouped into 12 age bins, with each lasting for 50 million years (Figure 1). We compared the mean values of $\delta^{34}S_{Eva}$ and $\delta^{34}S_{CAS}$ in each bin by using the *T*-test and bootstrapping methods. The results show that $\delta^{34}S_{Eva}$ is statistically higher than $\delta^{34}S_{CAS}$, i.e., $\Delta_{Eva\text{-}CAS} > 0$, in 600–550, 500–450, and 450–400 Ma bins, lower, i.e., $\Delta_{Eva\text{-}CAS} < 0$, in 550–500, 300–250, 250–200, 200–150, 100–50, and 50–0 Ma bins. Their mean values are indistinguishable, i.e., $\Delta_{Eva\text{-}CAS} \sim 0$, in 400–350, 350–300, and 150–100 Ma bins. In addition, $\Delta_{Eva\text{-}CAS}$ shows a clear decreasing trend from high positive values and becomes exclusively negative after 300 Ma (Figure 1b and c). This long-term declining trend is consistent with the higher temporal resolution statistical results from previous studies [23], but this trend has not been adequately explained in prior research.

DISCUSSIONS

The statistic difference between $\delta^{34}S_{CAS}$ and $\delta^{34}S_{Eva}$ data seems counterintuitive, because both carbonate and evaporite precipitations associate with negligible fractionation in S isotope (nearly 0‰ for CAS [24] and ~ +1 to +2‰ for evaporate [25]), and accordingly both proxies are widely used to reconstruct $\delta^{34}S_{SW}$ [19,24,26,27] unless $\delta^{34}S_{CAS}$ values were affected by non-CAS sulfate or modified in diagenesis. The difference between $\delta^{34}S_{Eva}$ and $\delta^{34}S_{CAS}$ cannot be attributed to either pyrite oxidation or non-CAS sulfate contaminations during the CAS extraction procedures [28,29], because such analytical errors should be universal for all analyzed samples of all geological ages, and thus cannot explain the decreasing trend of

$\Delta_{Eva\text{-}CAS}$ (Figure 1). Given evaporite and carbonate precipitations in different environment, i.e., near shore vs. bottom water [21,30], the systematic difference between $\delta^{34}S_{Eva}$ and $\delta^{34}S_{CAS}$ indeed reflects the discrepancies of marine S cycles in their depositional environment, or the depth gradient of $\delta^{34}S_{SW}$.

Errors in CAS and evaporite $\delta^{34}S$ records

In addition to the ideal case of S isotope records from seawater to CAS and evaporite, local seawater environments and diagenetic processes may also alter the relative differences in S isotopes between CAS and evaporite. There is a consensus that seawater sulfate has homogeneous S isotope values in the modern oxic open oceans [26,27]. However, local (either in seawater or porewater) sulfate isotopic composition ($\delta^{34}S_{SO_4}$) could be theoretically modified by (1) dissimilated sulfate reduction (DSR) that generates ^{34}S-depleted H_2S and elevates $\delta^{34}S_{SO_4}$, (2) pyrite precipitation that increases $\delta^{34}S_{SO_4}$, (3) oxidation of H_2S or sulfide (e.g., pyrite) that decreases $\delta^{34}S_{SO_4}$ [1,31], (4) fresh water seawater input with $\delta^{34}S_{SO_4}$ lower than seawater. These local reactions mainly affect $\delta^{34}S_{CAS}$ rather than $\delta^{34}S_{Eva}$ due to the following two reasons. First, both DSR and H_2S/sulfide oxidation occur within or at the top of sulfidic water column or the DSR zone in sediment, where evaporite cannot precipitate. Although freshwater sulfate input may have a more pronounced effect on evaporites deposited in nearshore regions [32,33], seawater sulfate concentrations remained higher than river water concentrations even in the early Phanerozoic when sulfate levels were lower than modern level [2,34]. Evaporite formation requires even higher sulfate concentrations. Therefore, freshwater sulfate input is unlikely to systematically influence the statistical results of seawater sulfate records. The standard deviation of evaporite sulfur isotope records remained relatively stable throughout the early Paleozoic [23]. This stable period spans the major oxygenation phases of the POE ocean and atmosphere [35,36], indicating that fluctuations in evaporite sulfur isotope records did not decrease as sulfate concentrations increased with atmospheric and oceanic oxygenation [2]. This observation supports the above viewpoint. Second, evaporite has much higher sulfate concentration than CAS, which makes it less vulnerable to post-depositional alterations or contaminations. In this framework, $\delta^{34}S_{CAS} > \delta^{34}S_{Eva}$ can be attributed to DSR or pyrite precipitation, whereas $\delta^{34}S_{CAS} < \delta^{34}S_{Eva}$ can be explained in terms of H_2S oxidation [37,38].

VOSC emission generated negative $\delta^{34}S_{SW}$ gradients

Negative $\delta^{34}S_{SW}$ gradients in non-sulfidic seawater was reported in comparing $\delta^{34}S_{CAS}$ for stratigraphic correlated sections in Middle Ordovician [38]. Thompson and Kah [38] explained the phenomenon by oxidation of H_2S from sulfidic water with a box model containing two boxes, sulfate and H_2S. However, it is important to note that a precondition for a box model is that the composition within a box should be homogeneous. While the $\delta^{34}S$ of sulfate is homogeneous in non-sulfidic seawater, it's heterogeneous in sulfidic seawater [1]. Therefore, there is at least 3 boxes in transportation of seawater S: sulfate in non-sulfidic seawater, sulfate in sulfidic seawater and H_2S in sulfidic seawater. The S transported to sulfate in non-sulfidic seawater box contains fluxes form sulfate in sulfidic seawater, with $\delta^{34}S$ of these two fluxes being linked because dissimilatory sulfate reduction prefers ^{32}S to form H_2S. A box model is not sufficient to figure out the overall $\delta^{34}S$ of S flux from sulfidic seawater.

As such, we've developed a 1D-DAR model to simulate the S exchange process. The quantitative S isotope exchange between sulfidic and non-sulfidic seawater should be rigorously tested by the process models. In addition, the VOSC cycle [15,16] has not been considered in previous studies. Here we developed a one-dimensional diffusion-advection-reaction (1D-DAR) model to simulate how concentration and S isotopes could be affected by DSR, H_2S oxidation, pyrite precipitation and VOSC formation (via the H_2S methylation pathway) and emission. The modeling results indicate that DSR and H_2S oxidation would modify the concentrations and isotopic compositions of both sulfate and H_2S, but do not change the contents and isotopes of total dissolved S ([TDS] and $\delta^{34}S_{TDS}$) (Figure 2a and b). In the model, TDS includes two components: sulfate and H_2S. Exchange mechanisms—diffusion and advection—affect both components equally. The conversion reaction between them sums to zero when combined as TDS. Therefore, TDS remains conservative at any position in the water column, provided no reaction converts TDS to non-dissolved components. Sulfur isotope fractionation during DSR controls the sulfur isotope composition of hydrogen sulfide that ultimately converts to pyrite [39]. In box models, DSR fractionation follows a Rayleigh fractionation process: sulfate reduces to hydrogen sulfide in a closed system, and the hydrogen sulfide is removed without further isotope exchange with sulfate [1,38]. In the 1D-DAR model, which accounts for spatial variation, the sulfate-hydrogen sulfide system still exhibits a Rayleigh fractionation curve [1]. The conservativeness of TDS is the essential prerequisite for describing this reaction through Rayleigh fractionation.

Both mathematical derivation and sensitivity tests (see Supplementary materials 3.3–4) demonstrate that this key conclusion is not affected by physical and chemical parameters such as diffusion constants, DSR reaction rates, and isotope fractionation, but rather is an inherent property of total dissolved sulfur within a closed system. Instead, the transformations of dissolved S (sulfate and H_2S) to gaseous (VOSC) or solid (pyrite) species would decrease [TDS] and increase $\delta^{34}S_{TDS}$ (Figure 2c–f). When pyrite or VOSC forms, TDS is no longer conservative, and additional sulfur isotope fractionation is superimposed onto the Rayleigh fractionation controlled by the hydrogen sulfide reduction ratio (Figure 3). For pyrite, the depositional process affects pyrite sulfur isotopes in a direction largely consistent with sulfur reduction. Greater pyrite deposition preferentially removes light sulfur isotopes from seawater, creating a downward-enriching isotope gradient in total dissolved sulfur that sustains additional transport of light isotopes. Although increased pyrite deposition makes pyrite sulfur isotopes slightly lighter than records with only trace pyrite deposition (Figure 3b), this effect is always much weaker than the sulfur reduction reaction itself (see the sulfur isotope gradient in non-sulfidic Black Sea waters [40,41]). For VOSC, however, the situation differs entirely. Because VOSC exists in gaseous form and migrates upward, it creates a downward-depleting sulfur isotope gradient above the VOSC oxidation interface. This gradient enriches pyrite sulfur isotopes (Figure 3c). Therefore, the sulfur isotope gradient we observe in non-sulfidic seawater corresponds to pyrite sulfur isotopes.

In another word, $\delta^{34}S_{CAS} > \delta^{34}S_{Eva}$ can be attributed to DSR, pyrite precipitation or VOSC formation and emission, but H_2S oxidation cannot lower $\delta^{34}S_{SO_4}$, regardless of whether H_2S is transported via diffusion, advection or redox boundary shifts. Except for H_2S oxidation, pyrite oxidation during sediment reworking [42] would also alter the $\delta^{34}S_{CAS}$ record. Although pyrite oxidation during sediment reworking would result in lower $\delta^{34}S_{CAS}$ data, most $\delta^{34}S_{CAS}$ data that immune from sediment reworking are still higher than $\delta^{34}S_{SW}$. The combined effect of pyrite precipitation and reoxidation in sediment reworking would still lead to higher average $\delta^{34}S_{CAS}$ values as compared with $\delta^{34}S_{SW}$, i.e., $\Delta_{Eva\text{-}CAS} < 0$, yet $\delta^{34}S_{CAS}$ data would show larger

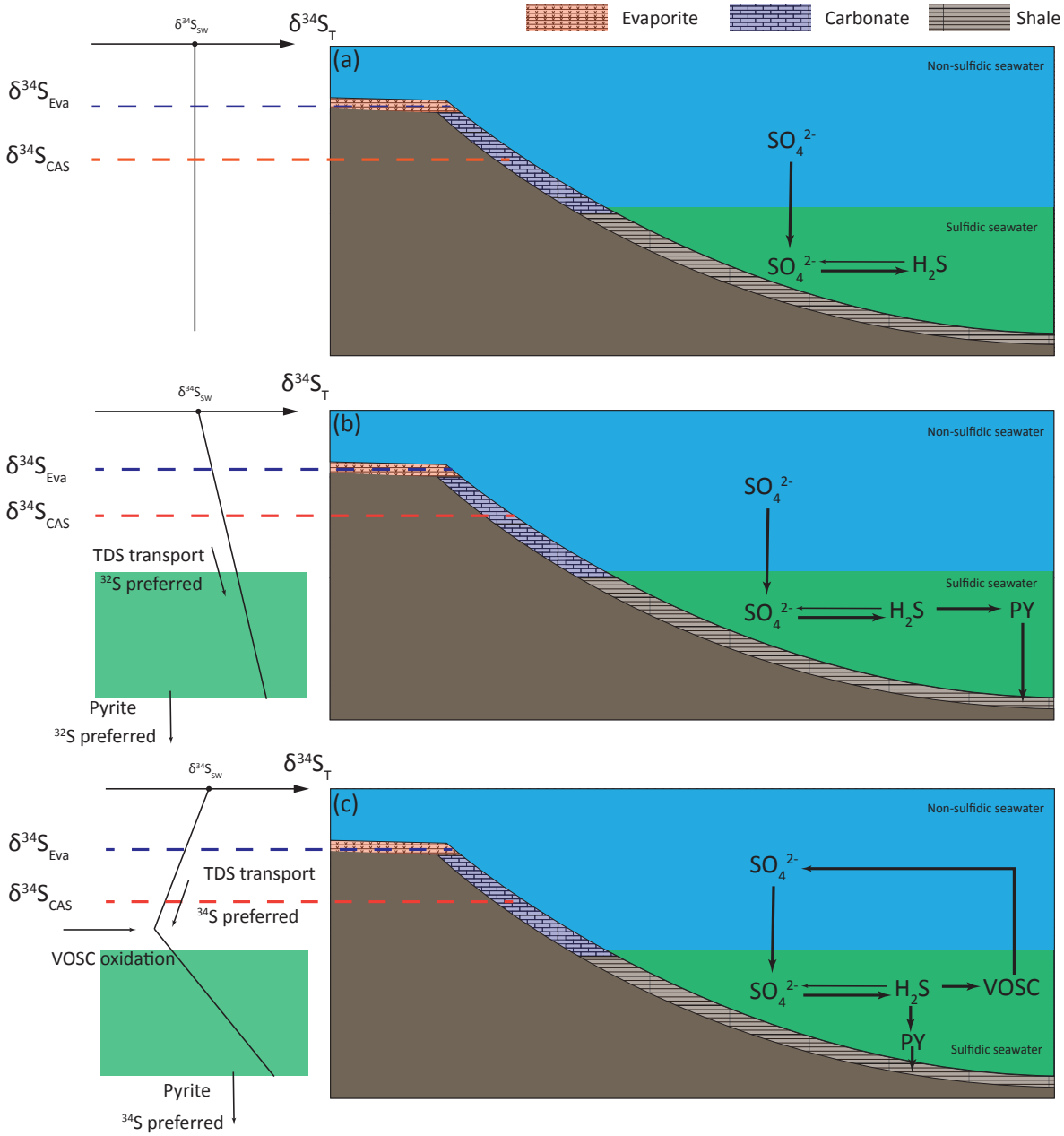


Figure 3 Sketch of how VOSC cycle affects $\delta^{34}S_{SW}$ gradient in non-sulfidic seawater and $\delta^{34}S_{py}$. Orange dashed lines represent the position average $\delta^{34}S_{Eva}$ recording $\delta^{34}S_{SW}$. Yellow dashed lines represent the position average $\delta^{34}S_{CAS}$ recording $\delta^{34}S_{SW}$. (a) Homogeneous $\delta^{34}S_{TDS}$ without pyrite sedimentation and VOSC formation. (b) Pyrite sedimentation results in slightly higher downward $\delta^{34}S_{SW}$ gradient in non-sulfidic seawater. (c) VOSC cycle results in lower downward $\delta^{34}S_{SW}$ gradient in non-sulfidic seawater and "superheavy pyrite".

standard deviation [23] given various degrees of sediment reworking.

Linking VOSC emission to "superheavy" pyrite

The local seawater S isotopes and early diagenetic alteration, which have been widely applied in previous S

isotope interpretation frameworks, cannot actually explain the long-term declining trend of $\Delta_{Eva\text{-}CAS}$, especially in the case of positive $\Delta_{Eva\text{-}CAS}$. Therefore, VOSC generation in sulfidic condition, followed by migration to and oxidation to ^{34}S-deplete sulfate in non-sulfidic water mass, is a possible solution for $\delta^{34}S_{CAS} < \delta^{34}S_{Eva}$ or positive $\Delta_{Eva\text{-}CAS}$ (Figure 3). In this case, $\delta^{34}S_{CAS} < \delta^{34}S_{Eva}$ or positive $\Delta_{Eva\text{-}CAS}$ can be used to indicate active VOSC cycle within sulfidic water mass.

Active VOSC cycles in the global scale require widespread sulfidic and DOC-enriched seawater, which are favored in limited ocean oxygenation [4,43], whereas weak VOSC cycles reveal pervasive ocean oxygenation or limited sulfidic seawater and/or formations of DOC-lean oceans. This may explain the general decreasing trend of $\Delta_{Eva\text{-}CAS}$ from positive to negative values and disappearance of "superheavy pyrite" [17], consistent with the long term oxygenation trend of the atmosphere-ocean system in the past 600 million years.

Gradual Paleozoic oxidation revealed by decline of VOSC emission

Now we retrieve the marine redox evolution in the past 600 million years. Between 600 and 550 Ma, the highest $\Delta_{Eva\text{-}CAS}$ and abundant "superheavy pyrites" indicate widespread sulfidic condition and seawater enriched in DOC [44–48]. The negative $\Delta_{Eva\text{-}CAS}$ values in 550–500 Ma might indicate temporary ocean oxidation, as inferred from other geochemical proxies [49]. The positive $\Delta_{Eva\text{-}CAS}$ values persist between 500 and 400 Ma, though lower than that of 600–550 Ma, implying the gradual reduction of VOSC cycles. The VOSC cycle might further decline with the onset of POE (Figure 1). Although "superheavy pyrite" was still observed occasionally, VOSC cycle may only be active in a few localities, resulting in an indistinguishable difference between $\delta^{34}S_{CAS}$ and $\delta^{34}S_{Eva}$. Persistent negative $\Delta_{Eva\text{-}CAS}$ since 300 Ma may imply disappearance of sulfidic condition and buildup of a DOC-lean ocean probably due to the complete ocean oxidation after POE [36]. Since then, the VOSC cycle via H_2S methylation pathway was entirely deactivated, instead VOSC cycle was dominated by the DMSP pathway with no isotopic effect on $\delta^{34}S_{SW}$ [50]. As such, $\delta^{34}S_{SW}$ is mainly controlled by the modern-style S cycle, i.e., DSR, pyrite burial, H_2S oxidation, and the DMSP pathway VOSC cycle [1].

Secular variations of the VOSC cycle as inferred from the S isotope records provide additional constraints on the marine redox evolution, particularly the extent of sulfidic continental margins, in the past 600 million years. Traditionally, the coverage of sulfidic seafloor has been inferred from the Mo concentration in black shales [7,51]. It is argued that the sulfidic seafloor of 1%–10% would be sufficient to scavenge seawater Mo resulting in low Mo concentration in black shales [9]. The compiled black shale data indicate the rise of Mo concentration after the Marinoan global glaciation [4,7], suggesting the decrease of sulfidic seafloor and oxidation of the oceans in the global scale. This argument is not inconsistent with other geochemical proxies showing periodic development of local or regional oceanic euxinia in Ediacaran and Cambrian oceans [52,53]. In fact, the ocean oxygenation is marked by the higher bound of Mo concentration [7], but low Mo concentrations of black shales do not imply local or regional oceanic euxinia. That is to say, Mo concentration makes no inference about the sulfidic condition after the Snowball Earth glaciations. Also, the connections between U, Mo concentrations and atmospheric O_2 level become much more complex [49]. In this study, we show that S isotopes of evaporite and CAS could be used to infer the extent of sulfidic condition of younger ages based on the compiled S isotope data (Figure 1). For example, the statistically

significant positive $\Delta_{Eva\text{-}CAS}$ before 400 Ma may be used to indicate the presence of substantive sulfidic seafloor even though the Mo concentration in seawater or black shales was already high.

Furthermore, NOE and POE are two oxygenation events [36,54], but it remains unclear whether there was a gradual increase since NOE or a sudden rise of the pO_2 level of atmosphere in POE. The S isotope data seem more consistent with the gradual oxygenation scenario as inferred from the diminish of the VOSC cycle between 500 and 400 Ma (Figure 1), while the onset of POE is identified as indistinguishable $\delta^{34}S_{Eva}$ and $\delta^{34}S_{CAS}$ data, presumably due to the diversification of vascular land plants since early Devonian [55,56]. Finally, the occurrence of negative $\Delta_{Eva\text{-}CAS}$ between 550 and 500 Ma (Figure 1) may hint an oxygenation window that broadly bracketed the early animal evolution and Cambrian explosion [32,33,57–59]. The reduction of sulfidic seafloor may correspond with the reduction of sulfate consumption and accordingly an increase of seawater sulfate concentration, which is supported by the Ba isotope data [60]. This unique oxygenation window in the Ediacaran-Cambrian transition may result from development of microbial mat in shallow marine seafloor (within euphotic zone) [61], which functioned as oxygenation oasis for benthic organisms [59,62], as well as the recovery of eukaryotic phytoplanktons in the open ocean [63–65], enhancing the efficiency of organic matter burial and accordingly leading to the oxidation of the surface Earth.

CONCLUSIONS

The reduction in the area of sulfidic seawater reflects the process of gradual oxidation of deep seawater between the two oxidation events (NOE-POE) until the complete evolution of the ocean. Although sulfur reduction reactions in seawater are accompanied by significant sulfur isotope fractionation, changes in the sulfur isotope record on a global scale are attributed to flux variations in the two major sinks of seawater sulfur: evaporites and pyrite. In local records, seawater sulfur isotope variations are attributed to hydrogen sulfide oxidation caused by upwelling of deep reducing seawater or fluctuations in the redox interface. We compiled the sulfur isotope differences between CAS and evaporites since 600 Ma and found that evaporite sulfur isotopes in the early Paleozoic were significantly heavier than CAS sulfur isotopes, with $\Delta_{Eva\text{-}CAS}$ showing an overall declining trend. Diagenetic alteration of CAS, recording errors in CAS and evaporite sulfur isotopes reflecting seawater sulfur isotopes, and analytical biases cannot fully explain the trend of evaporite sulfur isotopes being significantly heavier than CAS sulfur isotopes with a continuously declining difference. The 1D-DAR model demonstrates that the transport of dissolved sulfur, such as sulfate and hydrogen sulfide, cannot alter S isotopes in non-sulfidic seawater; only the transport and oxidation of gaseous (VOSC) and solid (pyrite) forms can produce downward-lightening sulfur isotope differences in non-sulfidic seawater. Considering the depositional environments of CAS and evaporites, VOSC emission and oxidation generated the downward negative S isotope gradient in non-sulfidic seawater during the early Paleozoic and earlier, which corresponds to the deposition of superheavy pyrite in the source-sink mass-isotope balance of sulfidic seawater. Therefore, the trend of evaporite sulfur isotopes being significantly heavier than CAS sulfur isotopes in the early Paleozoic with this difference decreasing over time indicates a reduction in the area of sulfidic water bodies or the DOC reservoir, which suppressed VOSC emission, revealing a gradual oxidation of the early Paleozoic ocean.

Funding

This work was supported by the National Natural Science Foundation of China (42225304, 42293291, 42503041), and the National Key Research and Development Program of China (2022YFF0800200).

Author contributions

T.H.: Conceptualization, methodology, software, formal analysis, writing–original draft, writing–review & editing, visualization, funding acquisition. B.S.: Conceptualization, resources, supervision, writing–original draft, writing–review & editing, funding acquisition.

Conflict of interest

The authors declare no conflict of interest.

References

1 Fike DA, Bradley AS, Rose CV. Rethinking the ancient sulfur cycle. *Annu Rev Earth Planet Sci* 2015; **43**: 593–622.
2 Canfield DE. The evolution of the Earth surface sulfur reservoir. *Am J Sci* 2004; **304**: 839–861.
3 Canfield DE. The early history of atmospheric oxygen: Homage to Robert M. Garrels. *Annu Rev Earth Planet Sci* 2005; **33**: 1–36.
4 Lyons TW, Diamond CW, Planavsky NJ, *et al.* Oxygenation, life, and the planetary system during Earth's middle history: An overview. *Astrobiology* 2021; **21**: 906–923.
5 Lyons TW, Reinhard CT, Planavsky NJ. The rise of oxygen in Earth's early ocean and atmosphere. *Nature* 2014; **506**: 307–315.
6 Anbar AD, Knoll AH. Proterozoic ocean chemistry and evolution: A bioinorganic bridge? *Science* 2002; **297**: 1137–1142.
7 Sahoo SK, Planavsky NJ, Jiang G, *et al.* Oceanic oxygenation events in the anoxic Ediacaran ocean. *Geobiology* 2016; **14**: 457–468.
8 Sahoo SK, Planavsky NJ, Kendall B, *et al.* Ocean oxygenation in the wake of the Marinoan glaciation. *Nature* 2012; **489**: 546–549.
9 Reinhard CT, Planavsky NJ, Robbins LJ, *et al.* Proterozoic ocean redox and biogeochemical stasis. *Proc Natl Acad Sci USA* 2013; **110**: 5357–5362.
10 Canfield DE, Farquhar J. The Global Sulfur Cycle. In: Knoll AH, Canfield DE, Konhauser KO, eds. *Fundamentals of Geobiology*. Chichester: John Wiley & Sons, Ltd, 2012, 49–64.
11 Brimblecombe P. The Global Sulfur Cycle. In: *Treatise on Geochemistry*. Heidelberg: Elsevier, 2014, 559–591.
12 Alcolombri U, Ben-Dor S, Feldmesser E, *et al.* Identification of the algal dimethyl sulfide-releasing enzyme: A missing link in the marine sulfur cycle. *Science* 2015; **348**: 1466–1469.
13 Levine NM. Putting the spotlight on organic sulfur. *Science* 2016; **354**: 418–419.
14 Kiene RP, Linn LJ. The fate of dissolved dimethylsulfoniopropionate (DMSP) in seawater: Tracer studies using 35S-DMSP. *Geochim Cosmochim Acta* 2000; **64**: 2797–2810.
15 Oduro H, Kamyshny Jr. A, Zerkle AL, *et al.* Quadruple sulfur isotope constraints on the origin and cycling of volatile organic sulfur compounds in a stratified sulfidic lake. *Geochim Cosmochim Acta* 2013; **120**: 251–262.
16 Amrani A, Said-Ahmad W, Shaked Y, *et al.* Sulfur isotope homogeneity of oceanic DMSP and DMS. *Proc Natl Acad Sci USA* 2013; **110**: 18413–18418.
17 Lang X, Zhao Z, Ma H, *et al.* Cracking the superheavy pyrite enigma: Possible roles of volatile organosulfur compound

emission. *Natl Sci Rev* 2021; **8**: nwab034.

18 Peng Y, Peng Y, Lang X, *et al.* Marine carbon-sulfur biogeochemical cycles during the steptoean positive carbon isotope excursion (SPICE) in the Jiangnan Basin, South China. *J Earth Sci* 2016; **27**: 242–254.

19 Crockford PW, Kunzmann M, Bekker A, *et al.* Claypool continued: Extending the isotopic record of sedimentary sulfate. *Chem Geol* 2019; **513**: 200–225.

20 Canfield DE, Farquhar J. Animal evolution, bioturbation, and the sulfate concentration of the oceans. *Proc Natl Acad Sci USA* 2009; **106**: 8123–8127.

21 Warren JK. Evaporites through time: Tectonic, climatic and eustatic controls in marine and nonmarine deposits. *Earth-Sci Rev* 2010; **98**: 217–268.

22 James NP, Kendall AC. Introduction to carbonate and evaporite facies models. In: Walker RG, James NP, eds. *Facies Models*, *Response to Sea Level Change*. St. Johns, NL: Geological Association of Canada, 1992, 265–275.

23 Present TM, Adkins JF, Fischer WW. Variability in sulfur isotope records of phanerozoic seawater sulfate. *Geophys Res Lett* 2020; **47**: e2020GL088766.

24 Lyons TW, Walter LM, Gellatly AM, *et al*. Sites of anomalous organic remineralization in the carbonate sediment of South Florida, USA: The sulfur cycle and carbonate-associated sulfate. In: Amend JP, Edwards KJ, Lyons TW, eds. *Sulfur Biogeochemistry: Past and Present (GSA Special Paper 379)*. Boulder: Geological Society of America, 2004, 161–176.

25 Raab M, Spiro B. Sulfur isotopic variations during seawater evaporation with fractional crystallization. *Chem Geol-Isotope Geosci Sect* 1991; **86**: 323–333.

26 Kampschulte A, Bruckschen P, Strauss H. The sulphur isotopic composition of trace sulphates in Carboniferous brachiopods: Implications for coeval seawater, correlation with other geochemical cycles and isotope stratigraphy. *Chem Geol* 2001; **175**: 149–173.

27 Kampschulte A, Strauss H. The sulfur isotopic evolution of Phanerozoic seawater based on the analysis of structurally substituted sulfate in carbonates. *Chem Geol* 2004; **204**: 255–286.

28 Peng Y, Bao H, Pratt LM, *et al.* Widespread contamination of carbonate-associated sulfate by present-day secondary atmospheric sulfate: Evidence from triple oxygen isotopes. *Geology* 2014; **42**: 815–818.

29 Marenco PJ, Corsetti FA, Hammond DE, *et al.* Oxidation of pyrite during extraction of carbonate associated sulfate. *Chem Geol* 2008; **247**: 124–132.

30 Tucker ME, Wright VP. *Carbonate Sedimentology*. Oxford: Blackwell Scientific, 1990.

31 Habicht KS, Canfield DE. Sulfur isotope fractionation during bacterial sulfate reduction in organic-rich sediments. *Geochim Cosmochim Acta* 1997; **61**: 5351–5361.

32 Zhang Y, Mills BJW, Newton RJ, *et al.* Orbitally-driven nutrient pulses linked to early Cambrian periodic oxygenation and animal radiation. *Geophys Res Lett* 2025; **52**: e2025GL118689.

33 He T, Zhu M, Mills BJW, *et al.* Possible links between extreme oxygen perturbations and the Cambrian radiation of animals. *Nat Geosci* 2019; **12**: 468–474.

34 Gill BC, Lyons TW, Saltzman MR. Parallel, high-resolution carbon and sulfur isotope records of the evolving Paleozoic marine sulfur reservoir. *Palaeogeogr Palaeoclimatol Palaeoecol* 2007; **256**: 156–173.

35 Wang H, Li C, Peng Y, *et al.* Two-billion-year transitional oxygenation of the Earth's surface. *Nature* 2025; **645**: 665–671.

36 Sperling EA, Wolock CJ, Morgan AS, *et al.* Statistical analysis of iron geochemical data suggests limited late Proterozoic oxygenation. *Nature* 2015; **523**: 451–454.

37 Kah LC, Thompson CK, Henderson MA, *et al.* Behavior of marine sulfur in the Ordovician. *Palaeogeogr*

Palaeoclimatol Palaeoecol 2016; **458**: 133–153.

38 Thompson CK, Kah LC. Sulfur isotope evidence for widespread euxinia and a fluctuating oxycline in Early to Middle Ordovician greenhouse oceans. *Palaeogeogr Palaeoclimatol Palaeoecol* 2012; **313-314**: 189–214.

39 Brimblecombe P, Heinrich DH, Karl KT. The global sulfur cycle. In: *Treatise on Geochemistry*. Oxford: Pergamon, 2003, 645–682.

40 Dubinin AV, Dubinina EO, Demidova TP, *et al.* Sulfur isotopes in the upper part of the Black Sea anoxic zone. *Oceanology* 2017; **57**: 797–805.

41 Jørgensen BB, Fossing H, Wirsen CO, *et al.* Sulfide oxidation in the anoxic Black Sea chemocline. *Deep Sea Res Part A Oceanographic Res Papers* 1991; **38**: S1083–S1103.

42 Pasquier V, Sansjofre P, Rabineau M, *et al.* Pyrite sulfur isotopes reveal glacial-interglacial environmental changes. *Proc Natl Acad Sci USA* 2017; **114**: 5941–5945.

43 Li C, Cheng M, Algeo TJ, *et al.* A theoretical prediction of chemical zonation in early oceans (>520 Ma). *Sci China Earth Sci* 2015; **58**: 1901–1909.

44 Jiang G, Kaufman AJ, Christie-Blick N, *et al.* Carbon isotope variability across the Ediacaran Yangtze platform in South China: Implications for a large surface-to-deep ocean $\delta^{13}C$ gradient. *Earth Planet Sci Lett* 2007; **261**: 303–320.

45 Li C, Planavsky NJ, Shi W, *et al.* Ediacaran marine redox heterogeneity and early animal ecosystems. *Sci Rep* 2015; **5**: 17097.

46 Tostevin R, He T, Turchyn AV, *et al.* Constraints on the late Ediacaran sulfur cycle from carbonate associated sulfate. *Precambrian Res* 2017; **290**: 113–125.

47 Shields GA, Mills BJW, Zhu M, *et al.* Unique Neoproterozoic carbon isotope excursions sustained by coupled evaporite dissolution and pyrite burial. *Nat Geosci* 2019; **12**: 823–827.

48 Dodd MS, Shi W, Li C, *et al.* Uncovering the Ediacaran phosphorus cycle. *Nature* 2023; **618**: 974–980.

49 Stockey RG, Cole DB, Farrell UC, *et al.* Sustained increases in atmospheric oxygen and marine productivity in the Neoproterozoic and Palaeozoic eras. *Nat Geosci* 2024; **17**: 667–674.

50 Amrani A. Organosulfur compounds: Molecular and isotopic evolution from biota to oil and gas. *Annu Rev Earth Planet Sci* 2014; **42**: 733–768.

51 Reinhard CT, Planavsky NJ, Lyons TW. Long-term sedimentary recycling of rare sulphur isotope anomalies. *Nature* 2013; **497**: 100–103.

52 Li C, Cheng M, Zhu M, *et al.* Heterogeneous and dynamic marine shelf oxygenation and coupled early animal evolution. *Emerg Top Life Sci* 2018; **2**: 279–288.

53 Jin C, Li C, Algeo TJ, *et al.* Highly heterogeneous “poikiloredox” conditions in the early Ediacaran Yangtze Sea. *Precambrian Res* 2018; **311**: 157–166.

54 Och LM, Shields-Zhou GA. The Neoproterozoic oxygenation event: Environmental perturbations and biogeochemical cycling. *Earth-Sci Rev* 2012; **110**: 26–57.

55 Kenrick P, Strullu-Derrien C. The origin and early evolution of roots. *Plant Physiol* 2014; **166**: 570–580.

56 Kenrick P, Crane PR. The origin and early evolution of plants on land. *Nature* 1997; **389**: 33–39.

57 Shu D. Cambrian explosion: Birth of tree of animals. *Gondwana Res* 2008; **14**: 219–240.

58 Brasier MD, Corfield RM, Derry LA, *et al.* Multiple $\delta_{13}C$ excursions spanning the Cambrian explosion to the Botomian crisis in Siberia. *Geology* 1994; **22**: 455–458.

59 Chen Z, Zhou C, Yuan X, *et al.* Death march of a segmented and trilobate bilaterian elucidates early animal evolution. *Nature* 2019; **573**: 412–415.

60 Wei W, Dong LH, Xiao S, *et al.* Seawater barium and sulfide removal improved marine habitability for the Cambrian Explosion of early animals. *Natl Sci Rev* 2024; **11**: nwae237.

61 Gehling JG. Microbial mats in terminal Proterozoic siliciclastics: Ediacaran death masks. *Palaios* 1999; **14**: 40–57.

62 Ding W, Dong L, Sun Y, *et al.* Early animal evolution and highly oxygenated seafloor niches hosted by microbial mats. *Sci Rep* 2019; **9**: 13628.

63 Dong L, Xiao S, Shen B, *et al.* Basal Cambrian microfossils from the Yangtze Gorges area (South China) and the Aksu area (Tarim block, northwestern China). *J Paleontol* 2009; **83**: 30–44.

64 Moczydlowska M. Early Cambrian phytoplankton radiations and appearance of metazoans. In: Peng S, Babcock LE, Zhu M, eds. *Cambrian System of South China (Palaeoworld No. 13)*. Hefei: University of Science and Technology of China Press, 2001, 293–296.

65 Tang Q, Zheng W, Zhang S, *et al.* Quantifying the global biodiversity of Proterozoic eukaryotes. *Science* 2024; **386**: eadm9137.